Supplementary Information

Electron scattering enhances orbital transport in amorphous Mn

Kyung-Hun Ko[1†], Daegeun Jo[2,3†], Peter M. Oppeneer[2,3], Hyun-Woo Lee[4,5] and Gyung-Min Choi[1⋆]

[1]Department of Energy Science, Sungkyunkwan University, Suwon 16419, Korea
[2]Department of Physics and Astronomy, Uppsala University, P.O. Box 516, SE-75120 Uppsala, Sweden
[3]Wallenberg Initiative Materials Science for Sustainability, Uppsala University, SE-75120 Uppsala, Sweden
[4]Department of Physics, Pohang University of Science and Technology, Pohang 37673, Korea
[5]Asia Pacific Center for Theoretical Physics, 77 Cheongam-ro, Pohang 37673, Korea

[†]These authors contributed equally.

[⋆]Correspondence to: gmchoi@skku.edu (G.-M. Choi)

Supplementary Note 1. Refractive index

Using spectroscopic ellipsometry (J.A. Woollam/M2000DI), we measured the complex refractive index ($\tilde{n} = n + ik$) over a wavelength (λ) range of 200–1000 nm (Fig. S1). At λ=780 nm, the values are 3.3+i2.7 (low-ρ), 3.1+i2.1 (mid-ρ), and 3.0+i1.9 (high-ρ).

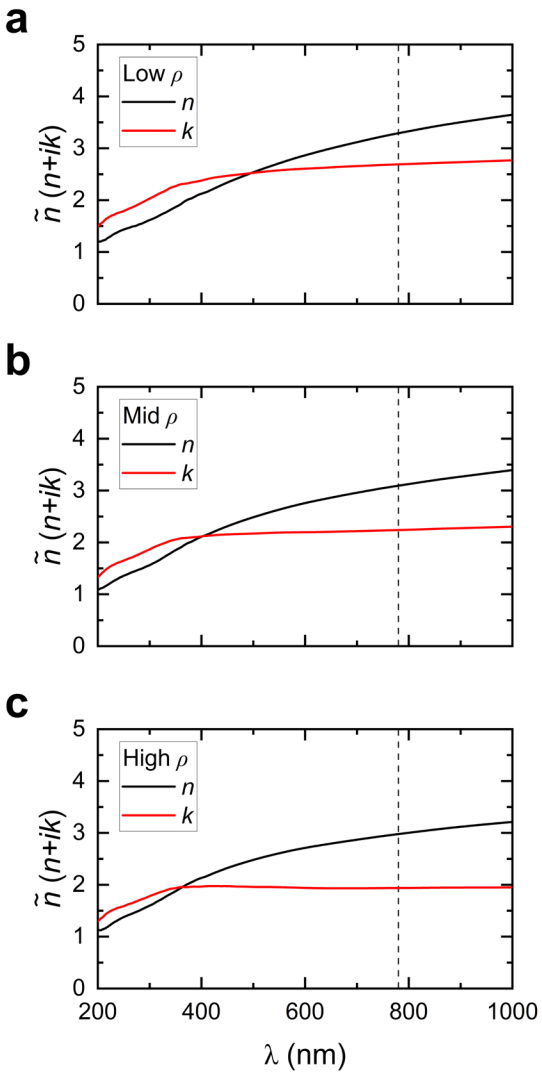

Fig. S1. Wavelength (λ) dependent complex refractive index ($\tilde{n}$) of Mn. a low-ρ, **b** mid-ρ, and **c** high-ρ. Black and red lines (n and k) are real and imaginary part of $\tilde{n}$.

Supplementary Note 2. X-ray diffraction measurements

Out-of-plane X-ray diffraction measurements were performed for Mn films with different resistivities (ρ), corresponding to the low ρ, mid ρ, high ρ samples (Fig. S2). In all samples, diffraction peaks were observed near 41.6˚, 64.5˚, and 90.8˚, which originate from the sapphire (0 0 0 6), (0 0 0 9), and (0 0 0 12), respectively.[1] Aside from these substrate peaks, no detectable diffraction peaks associated with Mn were observed over the measured range. These results suggest the absence of detectable long-range crystalline order in Mn films.

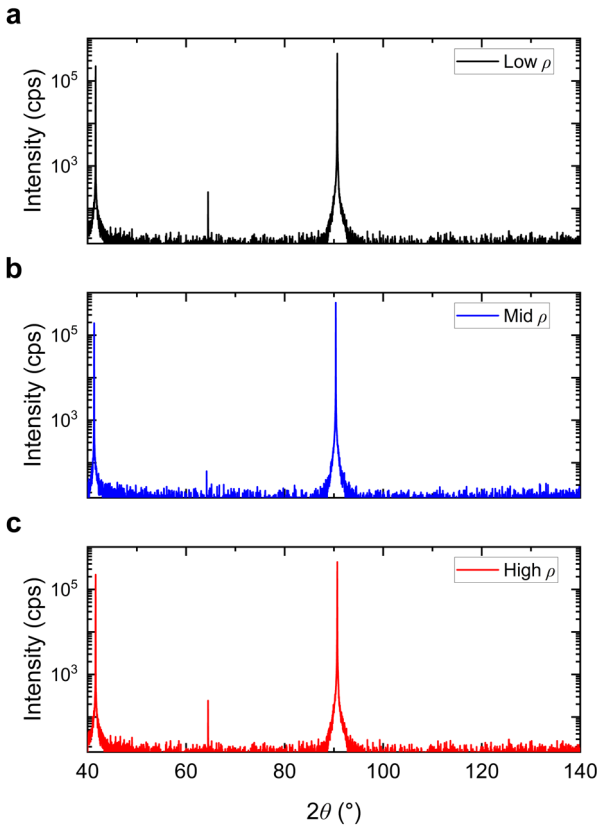

Fig. S2. Out-of-plane X-ray diffraction measurements of Mn films with different resistivities (ρ). a. low ρ, **b** mid ρ, and **c** high ρ. The peaks near 41.6˚, 64.5˚, and 90.8˚ originate from the sapphire (0 0 0 6), (0 0 0 9), and (0 0 0 12), respectively. No detectable Mn diffraction peaks are observed in any of the films.

Supplementary Note 3. Grain size estimation

The grain size of Mn was estimated from the radially averaged fast Fourier transform (FFT) intensity profile using the reciprocal-space form of the Scherrer equation, $D=K/\Delta g$, where D is the grain size, K is the shape factor, and Δg is the full width at half maximum (FWHM) of the FFT peak (Fig. S3).[2] The estimated grain size ranges from 2.6 to 6.9 nm depending on peak position, with an average of approximately 5 nm (Table 1).

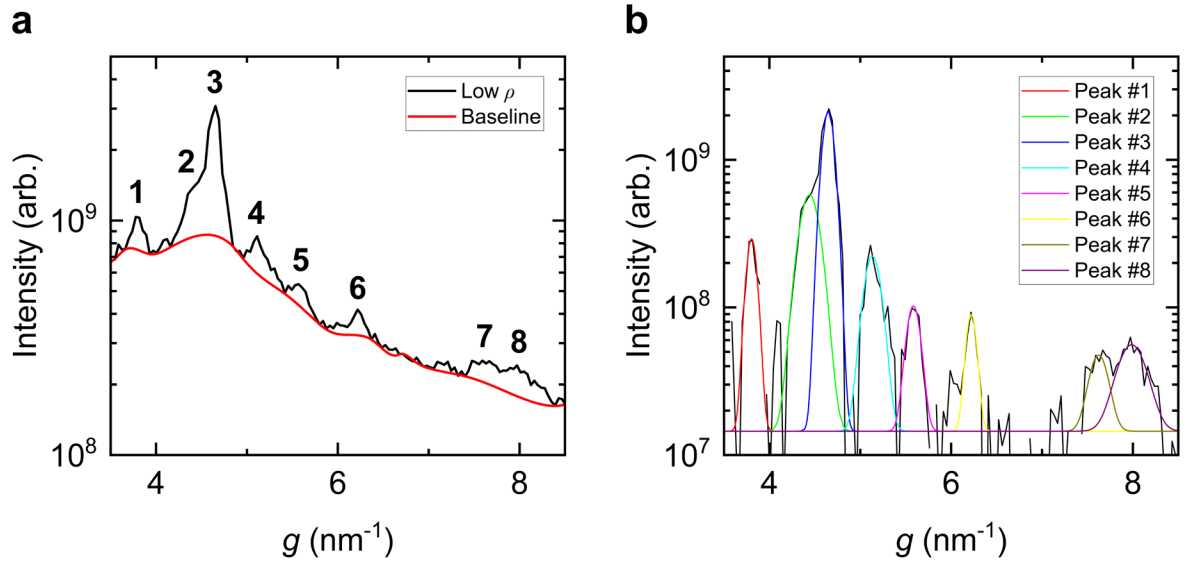

Fig. S3. Peak fitting of radially averaged FFT intensity. a. Radially averaged FFT intensity of low resistivity Mn (Black) together with the arbitrary baseline (Red). **b.** Peak fitting of the baseline-subtracted radially averaged FFT intensity. The numbers label the peaks in order of increasing scattering vector g.

	Peak 1	Peak 2	Peak 3	Peak 4	Peak 5	Peak 6	Peak 7	Peak 8
Center	3.80	4.44	4.65	5.13	5.58	6.22	7.62	7.99
FWHM	0.13	0.25	0.15	0.21	0.14	0.13	0.23	0.35
Grain (nm)	6.9	3.6	6	4.3	6.4	6.9	3.9	2.6

Table S1. Fitted peak parameters from the fitting of the radially averaged FFT intensity of low-resistivity Mn.

Supplementary Note 4. Fits to α-phase with different orbital relaxation lengths

Figure S4 shows fits using Q_{orbital} for α-Mn (Table 2 in the main text) by fixing l_{L} at 2 nm, 10 nm, and 40 nm while allowing M_0 to vary. Best fits are obtained with l_{L} of 10 nm for mid-ρ Mn and 2 nm for high-ρ Mn. Although the fitting does not fully capture the entire thickness dependence, the sign of $\mathrm{Im}(\tilde{\theta}_{\mathrm{K}})$ provides a criterion for estimating the upper limit of l_{L}. This is because $\mathrm{Im}(\tilde{\theta}_{\mathrm{K}})$ undergoes a sign inversion once l_{L} exceeds a critical value. For the mid-ρ and high-ρ Mn, this sign change occurs at l_{L}=14 nm and 4 nm, respectively, which we take as upper limits for α-Mn. The mid-ρ Mn therefore has l_{L} on the order of ~10 nm, which is consistent with the value obtained using Q_{emp} while the high-ρ Mn film exhibits a shorter l_{L} than the mid-ρ Mn.

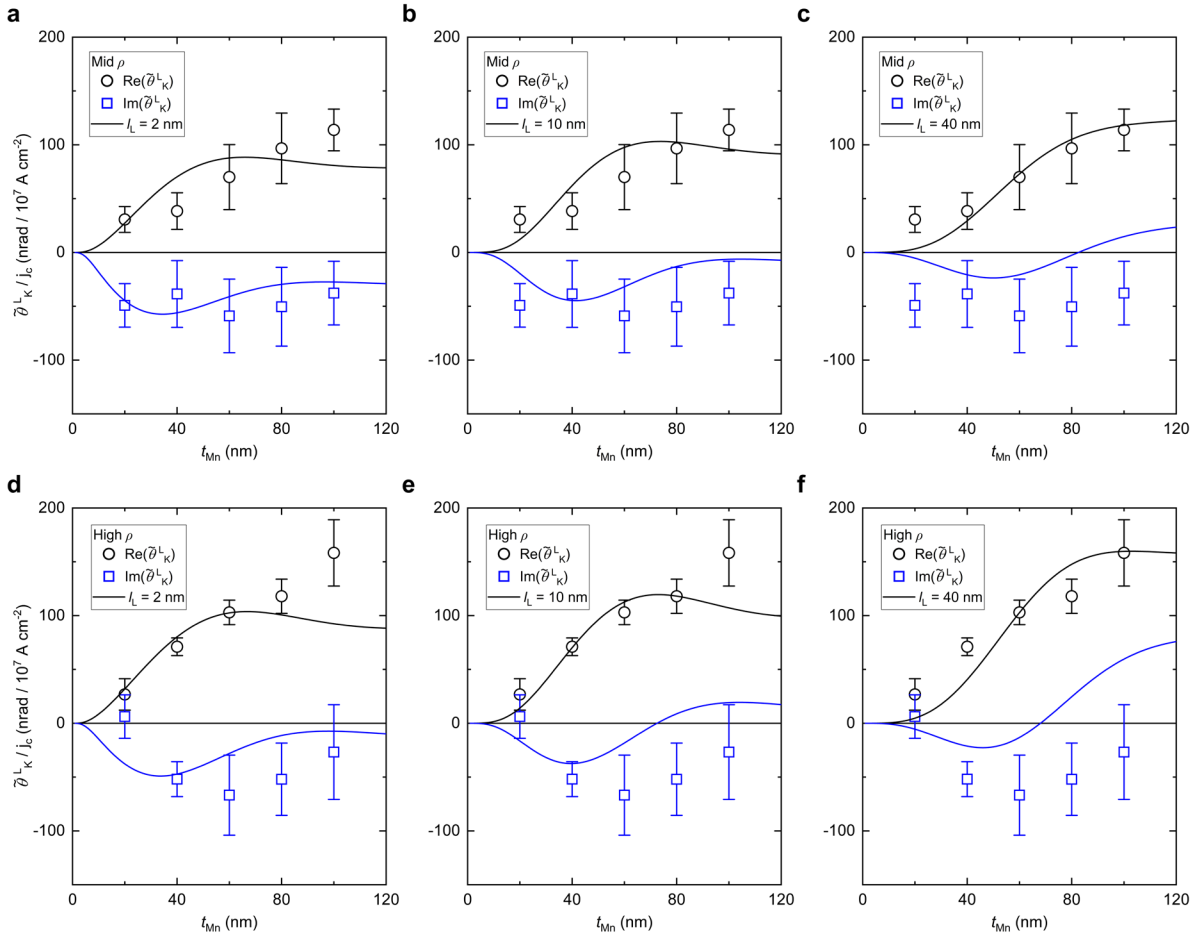

Fig. S4. Fits with different orbital relaxation lengths for α-phase Mn. Complex Kerr rotation angle per current density ($\tilde{\theta}^{L}_{K}/j_c$) measured for **a-c** mid-ρ and **d-e** high-ρ Mn films. Black circles and blue squares represent the Kerr rotation and ellipticity, $\mathrm{Re}[\tilde{\theta}^{L}_{K}]/j_c$ and $\mathrm{Im}[\tilde{\theta}^{L}_{K}]/j_c$, respectively. Solid lines are fits based on the theoretical calculation of the orbital Hall effect with **a** M_0=−(4.1±1.9) and l_L=2 nm; **b** M_0=−(1.2±0.4) and l_L=10 nm; **c** M_0=−(0.98±0.66) and l_L=40 nm; **d** M_0=−(3.3±1.6) and l_L=2 nm; **e** M_0=−(0.98±0.26) and l_L=10 nm; **f** M_0=−(0.97±0.67) and l_L=40 nm. M_0 is in units of 10^{-5} μ_B/atom per j_c=10^7 A/cm^2.

Supplementary Note 5. Fits to fcc and bcc structures with different orbital relaxation lengths.

Figure S5 shows fits using Q_{orbital} for fcc Mn (Table 2 in the main text) by fixing l_{L} at 2 nm, 10 nm, and 40 nm while allowing M_0 to vary. Because the ratio of real and imaginary components of Q_{orbital} for fcc Mn is similar to that of the α-phase, the overall trend of the fits resembles the α-phase. However, the sign inversion of $\mathrm{Im}(\tilde{\theta}_{\mathrm{K}})$ occurs at longer l_{L} in the fcc structure than α-phase. For the mid-ρ and high-ρ Mn, this sign change occurs at l_{L}=20 nm and 9 nm, respectively. Using the Q for α-phase, fcc structure, and empirical value consistently yield an l_{L} on the order of ~10 nm for the mid-ρ Mn, while the high-ρ Mn exhibits a shorter l_{L}.

Figure S6 represents fits using Q_{orbital} for the bcc structure by fixing l_{L} at 2 nm, 10 nm, and 40 nm while allowing M_0 to vary. In all cases, attempts to match the magnitude of $\mathrm{Im}\left[\tilde{\theta}_{\mathrm{K}}^{\mathrm{L}}\right]$ result in a substantially underestimated $\mathrm{Re}\left[\tilde{\theta}_{\mathrm{K}}^{\mathrm{L}}\right]$.

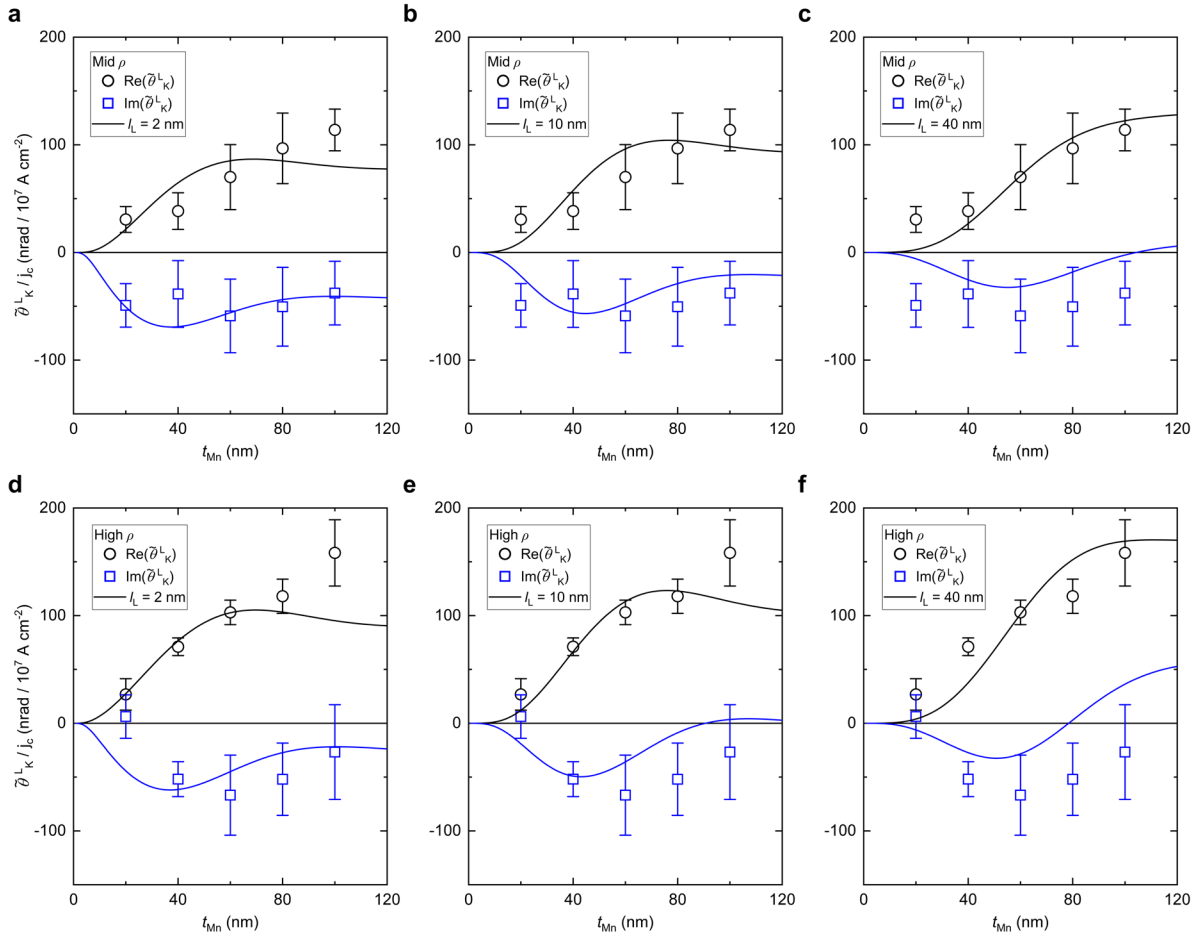

Fig. S5. Fits with different orbital relaxation lengths for fcc Mn. Complex Kerr rotation angle per current density ($\tilde{\theta}^{\mathrm{L}}_{\mathrm{K}}/j_{\mathrm{c}}$) measured for **a-c** mid-ρ and **d-e** high-ρ Mn films. Black circles and blue squares represent the Kerr rotation and ellipticity, $\mathrm{Re}\left[\tilde{\theta}^{\mathrm{L}}_{\mathrm{K}}\right]/j_{\mathrm{c}}$ and $\mathrm{Im}\left[\tilde{\theta}^{\mathrm{L}}_{\mathrm{K}}\right]/j_{\mathrm{c}}$, respectively. Solid lines are fits based on the theoretical calculation of the orbital Hall effect with **a** M_0=−(4.0±1.6) and l_{L}=2 nm; **b** M_0=−(1.2±0.35) and l_{L}=10 nm; **c** M_0=−(0.94±0.57) and l_{L}=40 nm; **d** M_0=−(3.3±1.4) and l_{L}=2 nm; **e** M_0=−(0.97±0.21) and l_{L}=10 nm; **f** M_0=−(0.93±0.62) and l_{L}=40 nm. M_0 is in units of 10^{-5} μ_{B}/atom per j_{c}=10^7 A/cm^2.

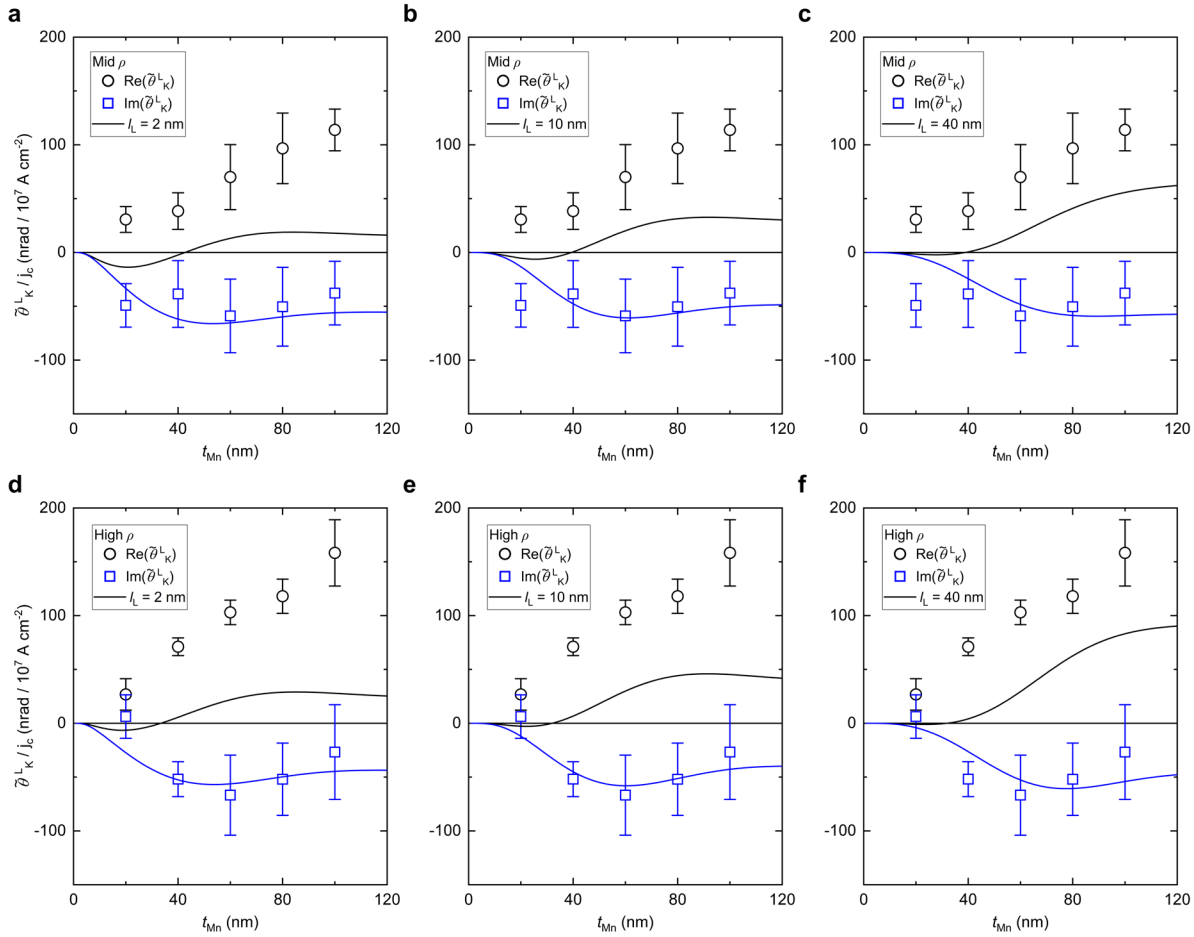

Fig. S6. Fits with different orbital relaxation lengths for bcc Mn. Complex Kerr rotation angle per current density ($\tilde{\theta}^{\mathrm{L}}_{\mathrm{K}}/j_{\mathrm{c}}$) measured for **a-c** mid-ρ and **d-e** high-ρ Mn films. Black circles and blue squares represent the Kerr rotation and ellipticity, $\mathrm{Re}\left[\tilde{\theta}^{\mathrm{L}}_{\mathrm{K}}\right]/j_{\mathrm{c}}$ and $\mathrm{Im}\left[\tilde{\theta}^{\mathrm{L}}_{\mathrm{K}}\right]/j_{\mathrm{c}}$, respectively. Solid lines are fits based on the theoretical calculation of the orbital Hall effect with **a** M_0=−(3.0±3.8) and l_{L}=2 nm; **b** M_0=−(0.8±0.8) and l_{L}=10 nm; **c** M_0=−(0.7±1.0) and l_{L}=40 nm; **d** M_0=−(2.0±4.5) and l_{L}=2 nm; **e** M_0=−(0.6±0.85) and l_{L}=10 nm; **f** M_0=−(0.6±1.6) and l_{L}=40 nm. M_0 is in units of 10^{-5} μ_{B}/atom per j_{c}=10^7 A/cm^2.

Supplementary Note 6. Theoretical calculation of the proper orbital Hall conductivity

For the calculation of the proper orbital Hall conductivity, we considered nonmagnetic Mn films consisting of 15 atomic layers with fcc(111) and bcc(110) orientations. The structures and lattice constants for each system are shown in Figs. S5a and S5b. The electronic structures for each structure were obtained by the density functional theory code FLEUR[3,4] based on the full-potential linearized augmented plane-wave method.[5] The film mode in the FLEUR code was employed, and the two-dimensional Brillouin zone was sampled using 16×16 Monkhorst-Pack **k**-mesh.[6] The Perdew-Burke-Ernzerhof functional within the generalized gradient approximation was used for an exchange-correlation functional,[7] and the spin-orbit coupling was included within the second variation scheme.[8]

Using the obtained Bloch eigenstates, maximally localized Wannier functions (MLWFs) were constructed using WANNIER90 code.[9,10] The number of MLWFs is 18 for each atomic layer, with initial projections onto *s*, *p*, and *d* orbitals. For the disentanglement procedure, the frozen window energy maximum was set to 5 eV above the Fermi energy. With the MLWFs, the Hamiltonian ($\hat{H}$), orbital angular momentum (OAM) ($\hat{\mathbf{L}}$), and position ($\hat{\mathbf{r}}$) operators are interpolated onto a dense **k**-mesh, where the OAM is treated within the atom-centered approximation.

The orbital Hall conductivity, which relates the orbital current flowing in the *z* direction to an electric field along the *x* direction, was evaluated from the Kubo formula:[11,12]

$$\sigma_{\mathrm{OH}} = \frac{e\hbar}{t_{\mathrm{Mn}}} \int \frac{d^2\mathbf{k}}{(2\pi)^2} \sum_{n\neq m} (f_{n\mathbf{k}} - f_{m\mathbf{k}}) \mathrm{Im} \left[\frac{\left\langle \psi_{n\mathbf{k}} \middle| \hat{j}_z^{L_y} \middle| \psi_{m\mathbf{k}} \right\rangle \langle \psi_{m\mathbf{k}} | \hat{v}_x | \psi_{n\mathbf{k}} \rangle}{(\epsilon_{nk} - \epsilon_{mk})(\epsilon_{nk} - \epsilon_{mk} + i\Gamma)} \right], \tag{S1}$$

where $|\psi_{n\mathbf{k}}\rangle$ and $\epsilon_{n\mathbf{k}}$ are the eigenstate and the energy eigenvalue for band *n*, respectively, $f_{n\mathbf{k}}$ is the Fermi-Dirac distribution function, $\hat{\mathbf{v}} = [\hat{\mathbf{r}}, \hat{H}]/i\hbar$ is the velocity operator, and the broadening energy Γ was set to 0.1 eV. Dividing by the film thickness t_{Mn} yields the unit of the bulk orbital Hall conductivity. For the orbital current operator $\hat{j}_z^{L_y}$, the use of the conventional form $\hat{j}_z^{\mathrm{con},L_y} = \frac{1}{2}\{\hat{v}_z, \hat{L}_y\}$ gives the conventional orbital Hall conductivity $\sigma_{\mathrm{OH}}^{\mathrm{con}}$.[10,11] However, since OAM is not a conserved quantity, $\hat{j}_z^{\mathrm{con},L_y}$ does not satisfy the continuity equation and instead obeys

$$\frac{\partial \hat{L}_y(\mathbf{r})}{\partial t} + \hat{j}_z^{\mathrm{con},L_y} = \hat{T}^{L_y}, \tag{S2}$$

where the source or sink term $\hat{T}^{L_y} = [\hat{L}_y, \hat{H}]/i\hbar$ represents the torque exerted on OAM.[13,14] Note that $\hat{T}^{L_y}$ is nonzero if the Hamiltonian does not commute with $\hat{L}_y$, which is mainly due to the crystal potential when spin-orbit coupling is weak. Therefore, $\sigma_{\mathrm{OH}}^{\mathrm{con}}$ is not directly related to the accumulation of OAM at the sample. To obtain the proper orbital Hall conductivity $\sigma_{\mathrm{OH}}^{\mathrm{pro}}$, which is linked to OAM accumulation, the proper orbital current operator must be used, given by[13,14]

$$\hat{J}_z^{\mathrm{pro},L_y} = \hat{J}_z^{\mathrm{con},L_y} + \hat{P}_z^{L_y}, \tag{S3}$$

where $\hat{P}_z^{L_y} = \frac{1}{2}\{\hat{z}, \hat{T}^{L_y}\}$ is the torque dipole operator, whose expression is valid only after integrating over the sample with inversion symmetry. The inclusion of $\hat{P}_z^{L_y}$ allows $\hat{J}_z^{\mathrm{pro},L_y}$ to satisfy the continuity equation $\frac{\partial \hat{L}_y(\mathbf{r})}{\partial t} + \hat{J}_z^{\mathrm{pro},L_y} = 0$ and thus properly describe orbital accumulation. By substituting $\hat{J}_z^{\mathrm{pro},L_y}$ given in Eq. (S3) for $\hat{J}_z^{L_y}$ in Eq. (S1), the proper orbital Hall conductivity $\sigma_{\mathrm{OH}}^{\mathrm{pro}}$ is obtained.

Fig. S7. Crystal structures of Mn films with a fcc(111) and b bcc(110) orientations. The bulk lattice constants a_{fcc}=3.5 Å and a_{bcc}=2.8 Å are used for the fcc and bcc structures,[15] respectively.

References

1 Inaba, K. Characterization of GaN-related materials using high-resolution XRD. *Rigaku J.* **30**, 7–16 (2014).

2. Kukleva, E. *et al*. Surface protolytic property characterization of hydroxyapatite and titanium dioxide nanoparticles. *RSC Adv.* **9**, 21989–21995 (2019).

3. The FLEUR project. http://www.flapw.de/.

4. Wortmann, D. *et al.* FLEUR. Zenodo https://doi.org/10.5281/zenodo.7576163 (2024).

5. Monkhorst, H. J. & Pack, J. D. Special points for Brillouin-zone integrations. *Phys. Rev. B* **13**, 5188–5192 (1976).

6. Wimmer, E., Krakauer, H., Weinert, M. & Freeman, A. J. Full-potential self-consistent linearized-augmented-plane-wave method for calculating the electronic structure of molecules and surfaces: O_2 molecule. *Phys. Rev. B* **24**, 864–875 (1981).

7. Perdew, J. P., Burke, K. & Ernzerhof, M. Generalized gradient approximation made simple. *Phys. Rev. Lett.* **77**, 3865–3868 (1996).

8. Li, C., Freeman, A. J., Jansen, H. J. F. & Fu, C. L. Magnetic anisotropy in low-dimensional ferromagnetic systems: Fe monolayers on Ag(001), Au(001), and Pd(001) substrates. *Phys. Rev. B* **42**, 5433–5442 (1990).

9. Pizzi, G. *et al*. Wannier90 as a community code: new features and applications. *J. Phys.: Condens. Matter* **32**, 165902 (2020).

10. Freimuth, F., Mokrousov, Y., Wortmann, D., Heinze, S. & Blügel, S. Maximally localized Wannier functions within the FLAPW formalism. *Phys. Rev. B* **78**, 035120 (2008).

11. Go, D., Jo, D., Kim, C. & Lee, H.-W. Intrinsic spin and orbital Hall effects from orbital texture. *Phys. Rev. Lett*. **121**, 086602 (2018).

12. Jo, D., Go, D. & Lee, H.-W. Gigantic intrinsic orbital Hall effects in weakly spin-orbit coupled metals. *Phys. Rev. B* **98**, 214405 (2018).

13. Choi, Y.-G. et al. Observation of the orbital Hall effect in a light metal Ti. *Nature* **619**, 52–56 (2023).

14. Go, D., Seifert, T. S., Kampfrath, T., Ando, K., Lee, H.-W. & Mokrousov, Y. Local and Global Reciprocity in Orbital-Charge-Coupled Transport. Preprint at https://arxiv.org/abs/2407.00517 (2024).

15. Fuster, G. et al. Magnetism in bcc and fcc manganese. *Phys. Rev. B* **38**, 423–432 (1988).